Research Article | Vol. 8, No. 1 | 1 Jan 2017 | BIOMEDICAL OPTICS EXPRESS 420

Biomedical Optics EXPRESS

Wide field and highly sensitive angiography based on optical coherence tomography with akinetic swept source

JINGJIANG XU, SHAOZHEN SONG, WEI WEI, AND RUIKANG K. WANG*

University of Washington, Department of Bioengineering, Seattle, Washington 98195, USA
**wangrk@uw.edu*

Abstract: Wide-field vascular visualization in bulk tissue that is of uneven surface is challenging due to the relatively short ranging distance and significant sensitivity fall-off for most current optical coherence tomography angiography (OCTA) systems. We report a long ranging and ultra-wide-field OCTA (UW-OCTA) system based on an akinetic swept laser. The narrow instantaneous linewidth of the swept source with its high phase stability, combined with high-speed detection in the system enable us to achieve long ranging (up to 46 mm) and almost negligible system sensitivity fall-off. To illustrate these advantages, we compare the basic system performances between conventional spectral domain OCTA and UW-OCTA systems and their functional imaging of microvascular networks in living tissues. In addition, we show that the UW-OCTA is capable of different depth-ranging of cerebral blood flow within entire brain in mice, and providing unprecedented blood perfusion map of human finger in *vivo*. We believe that the UW-OCTA system has promises to augment the existing clinical practice and explore new biomedical applications for OCT imaging.

OCIS codes: (110.4500) Optical coherence tomography; (170.3880) Medical and biological imaging; (170.0110) Imaging systems; (140.3600) Lasers, tunable; (170.2655) Functional monitoring and imaging.

References and links

1. R. K. Wang, S. L. Jacques, Z. Ma, S. Hurst, S. R. Hanson, and A. Gruber, "Three dimensional optical angiography," Opt. Express **15**(7), 4083–4097 (2007).
2. T. E. de Carlo, A. Romano, N. K. Waheed, and J. S. Duker, "A review of optical coherence tomography angiography (OCTA)," Int. J. Retina Vitreous **1**(1), 5 (2015).
3. R. K. Wang, L. An, S. Saunders, and D. J. Wilson, "Optical microangiography provides depth-resolved images of directional ocular blood perfusion in posterior eye segment," J. Biomed. Opt. **15**, 020502 (2010).
4. A. Mariampillai, B. A. Standish, E. H. Moriyama, M. Khurana, N. R. Munce, M. K. K. Leung, J. Jiang, A. Cable, B. C. Wilson, I. A. Vitkin, and V. X. D. Yang, "Speckle variance detection of microvasculature using swept-source optical coherence tomography," Opt. Lett. **33**(13), 1530–1532 (2008).
5. J. Fingler, D. Schwartz, C. Yang, and S. E. Fraser, "Mobility and transverse flow visualization using phase variance contrast with spectral domain optical coherence tomography," Opt. Express **15**(20), 12636–12653 (2007).
6. Y. Jia, O. Tan, J. Tokayer, B. Potsaid, Y. Wang, J. J. Liu, M. F. Kraus, H. Subhash, J. G. Fujimoto, J. Hornegger, and D. Huang, "Split-spectrum amplitude-decorrelation angiography with optical coherence tomography," Opt. Express **20**(4), 4710–4725 (2012).
7. J. Enfield, E. Jonathan, and M. Leahy, "In vivo imaging of the microcirculation of the volar forearm using correlation mapping optical coherence tomography (cmOCT)," Biomed. Opt. Express **2**(5), 1184–1193 (2011).
8. A. Zhang, Q. Zhang, C. L. Chen, and R. K. K. Wang, "Methods and algorithms for optical coherence tomography-based angiography: a review and comparison," J. Biomed. Opt. **20**(10), 100901 (2015).
9. L. An, J. Qin, and R. K. Wang, "Ultrahigh sensitive optical microangiography for in vivo imaging of microcirculations within human skin tissue beds," Opt. Express **18**(8), 8220–8228 (2010).
10. V. J. Srinivasan, J. Y. Jiang, M. A. Yaseen, H. Radhakrishnan, W. Wu, S. Barry, A. E. Cable, and D. A. Boas, "Rapid volumetric angiography of cortical microvasculature with optical coherence tomography," Opt. Lett. **35**(1), 43–45 (2010).
11. Y. Jia, L. An, and R. K. K. Wang, "Label-free and highly sensitive optical imaging of detailed microcirculation within meninges and cortex in mice with the cranium left intact," J. Biomed. Opt. **15**(3), 030510 (2010).
12. T.-H. Tsai, O. O. Ahsen, H.-C. Lee, K. Liang, M. Figueiredo, Y. K. Tao, M. G. Giacomelli, B. M. Potsaid, V. Jayaraman, Q. Huang, A. E. Cable, J. G. Fujimoto, and H. Mashimo, "Endoscopic optical coherence angiography enables 3-dimensional visualization of subsurface microvasculature," Gastroenterology **147**(6), 1219–1221 (2014).

#277560 http://dx.doi.org/10.1364/BOE.8.000420
Journal © 2017 Received 26 Sep 2016; revised 15 Dec 2016; accepted 18 Dec 2016; published 22 Dec 2016

Biomedical Optics EXPRESS

13. S.-W. Lee, H.-W. Jeong, B.-M. Kim, Y.-C. Ahn, W. Jung, and Z. Chen, "Optimization for axial resolution, depth range, and sensitivity of spectral domain optical coherence tomography at 1.3 μm," J. Korean Phys. Soc. **55**(6), 2354–2360 (2009).
14. P. H. Tomlins and R. Wang, "Theory, developments and applications of optical coherence tomography," J. Phys. D Appl. Phys. **38**(15), 2519–2535 (2005).
15. P. Li, M. Johnstone, and R. K. Wang, "Full anterior segment biometry with extended imaging range spectral domain optical coherence tomography at 1340 nm," J. Biomed. Opt. **19**(4), 046013 (2014).
16. Q. Q. Zhang, C. S. Lee, J. Chao, C. L. Chen, T. Zhang, U. Sharma, A. Q. Zhang, J. Liu, K. Rezaei, K. L. Pepple, R. Munsen, J. Kinyoun, M. Johnstone, R. N. Van Gelder, and R. K. K. Wang, "Wide-field optical coherence tomography based microangiography for retinal imaging," Sci. Rep. **6,** 22017 (2016).
17. J. Xu, W. Wei, S. Song, X. Qi, and R. K. Wang, "Scalable wide-field optical coherence tomography-based angiography for in vivo imaging applications," Biomed. Opt. Express **7**(5), 1905–1919 (2016).
18. W. Drexler and J. G. Fujimoto, "Optical Coherence Tomography: Technology and Applications (Biological and Medical Physics, Biomedical Engineering)," Springer (2008).
19. I. Grulkowski, J. J. Liu, B. Potsaid, V. Jayaraman, C. D. Lu, J. Jiang, A. E. Cable, J. S. Duker, and J. G. Fujimoto, "Retinal, anterior segment and full eye imaging using ultrahigh speed swept source OCT with vertical-cavity surface emitting lasers," Biomed. Opt. Express **3**(11), 2733–2751 (2012).
20. W. Y. Oh, B. J. Vakoc, M. Shishkov, G. J. Tearney, and B. E. Bouma, ">400 kHz repetition rate wavelength-swept laser and application to high-speed optical frequency domain imaging," Opt. Lett. **35**(17), 2919–2921 (2010).
21. R. Huber, M. Wojtkowski, and J. G. Fujimoto, "Fourier Domain Mode Locking (FDML): A new laser operating regime and applications for optical coherence tomography," Opt. Express **14**(8), 3225–3237 (2006).
22. T. H. Tsai, B. Potsaid, Y. K. Tao, V. Jayaraman, J. Jiang, P. J. S. Heim, M. F. Kraus, C. Zhou, J. Hornegger, H. Mashimo, A. E. Cable, and J. G. Fujimoto, "Ultrahigh speed endoscopic optical coherence tomography using micromotor imaging catheter and VCSEL technology," Biomed. Opt. Express **4**(7), 1119–1132 (2013).
23. D. J. Fechtig, B. Grajciar, T. Schmoll, C. Blatter, R. M. Werkmeister, W. Drexler, and R. A. Leitgeb, "Line-field parallel swept source MHz OCT for structural and functional retinal imaging," Biomed. Opt. Express **6**(3), 716–735 (2015).
24. W. Wieser, B. R. Biedermann, T. Klein, C. M. Eigenwillig, and R. Huber, "Multi-Megahertz OCT: High quality 3D imaging at 20 million A-scans and 4.5 GVoxels per second," Opt. Express **18**(14), 14685–14704 (2010).
25. J. Xu, X. Wei, L. Yu, C. Zhang, J. Xu, K. K. Wong, and K. K. Tsia, "High-performance multi-megahertz optical coherence tomography based on amplified optical time-stretch," Biomed. Opt. Express **6**(4), 1340–1350 (2015).
26. J. Xu, C. Zhang, J. Xu, K. K. Wong, and K. K. Tsia, "Megahertz all-optical swept-source optical coherence tomography based on broadband amplified optical time-stretch," Opt. Lett. **39**(3), 622–625 (2014).
27. I. Grulkowski, J. J. Liu, B. Potsaid, V. Jayaraman, J. Jiang, J. G. Fujimoto, and A. E. Cable, "High-precision, high-accuracy ultralong-range swept-source optical coherence tomography using vertical cavity surface emitting laser light source," Opt. Lett. **38**(5), 673–675 (2013).
28. M.-T. Tsai, T.-T. Chi, H.-L. Liu, F.-Y. Chang, C.-H. Yang, C.-K. Lee, and C.-C. Yang, "Microvascular imaging using swept-source optical coherence tomography with single-channel acquisition," Appl. Phys. Express **4**(9), 097001 (2011).
29. M. Bonesi, M. P. Minneman, J. Ensher, B. Zabihian, H. Sattmann, P. Boschert, E. Hoover, R. A. Leitgeb, M. Crawford, and W. Drexler, "Akinetic all-semiconductor programmable swept-source at 1550 nm and 1310 nm with centimeters coherence length," Opt. Express **22**(3), 2632–2655 (2014).
30. H. C. Hendargo, R. P. McNabb, A.-H. Dhalla, N. Shepherd, and J. A. Izatt, "Doppler velocity detection limitations in spectrometer-based versus swept-source optical coherence tomography," Biomed. Opt. Express **2**(8), 2175–2188 (2011).
31. L. Shi, J. Qin, R. Reif, and R. K. Wang, "Wide velocity range Doppler optical microangiography using optimized step-scanning protocol with phase variance mask," J. Biomed. Opt. **18**(10), 106015 (2013).
32. R. K. Wang and L. An, "Doppler optical micro-angiography for volumetric imaging of vascular perfusion in vivo," Opt. Express **17**(11), 8926–8940 (2009).
33. R. K. K. Wang, X. Q. Xu, V. V. Tuchin, and J. B. Elder, "Concurrent enhancement of imaging depth and contrast for optical coherence tomography by hyperosmotic agents," J. Opt. Soc. Am. B **18**(7), 948–953 (2001).
34. R. K. Wang, A. Zhang, W. J. Choi, Q. Zhang, C. L. Chen, A. Miller, G. Gregori, and P. J. Rosenfeld, "Wide-field optical coherence tomography angiography enabled by two repeated measurements of B-scans," Opt. Lett. **41**(10), 2330–2333 (2016).
35. Z. Chen, M. Liu, M. Minneman, L. Ginner, E. Hoover, H. Sattmann, M. Bonesi, W. Drexler, and R. A. Leitgeb, "Phase-stable swept source OCT angiography in human skin using an akinetic source," Biomed. Opt. Express **7**(8), 3032–3048 (2016).

1. Introduction

Optical coherence tomography based angiography (OCTA) is becoming increasingly important in the clinical translation for the purpose of imaging vascular involvements in pathological diseases, e.g. ophthalmology. OCTA utilizes the intrinsic motion contrast due to dynamic moving particles (e.g. red blood cells) to differentiate functional blood vessels from

Biomedical Optics EXPRESS

static tissue background [1]. Compared to conventional angiography such as fluorescein angiography (FA) and indocyanine green angiography (ICGA) that are time consuming, dye-based and invasive, OCTA is fast, safe and non-invasive in providing information about three-dimensional (3D) tissue vascular networks with high contrast, high resolution and high speed. These attributes have made OCTA to be rapidly adopted in ophthalmology for the evaluation of common ophthalmologic diseases such as glaucoma, diabetic retinopathy, and age related macular degeneration (AMD) [2]. A variety of processing algorithms including optical micro-angiography (OMAG) [3], speckle variance [4], phase variance [5], split-spectrum amplitude decorrelation angiography (SSADA) [6], and correlation mapping [7] have been developed to create high-contrast blood flow perfusion map [8]. The imaging protocol of ultra-high sensitive OMAG based on repeated B-scanning protocol enables unprecedented flow sensitivity down to capillary level, providing detailed examination for blood microcirculation [9, 10]. With its rapid development, the clinical applications of OCTA have currently seen a move from ophthalmology to other biomedical fields such as neuroscience [11], dermatology [9], and gastroenterology [12].

To date, the spectral-domain OCT (SD-OCT) configuration based on the detection scheme of spectrometer is the most mature and the main stay for clinical translations. The advantage of spectral domain configuration is its high stability of OCT signals, including its intensity (magnitude) and phase, which facilitates to achieve the motion contrast due to blood flow. However, when picturing the target sample, there are a number of limitations associated with the current SD-OCT. First of all, the spectral resolution due to spectrometer detection is inherently limited, which would have at least two consequences: 1) relatively short ranging distance, and 2) rapid fall-off of the system sensitivity along the imaging depth. The spectral resolution in SD-OCT is determined by the optical setup in the detection arm where the spectrometer is situated. The parameters that are important to consider include, among other factors, the beam size, the grating employed, and the number of active pixels available in the line scan camera. While these parameters can be theoretically optimized, they lead to a significant sensitivity fall-off within a few millimeters of the ranging distance in practical implementations [13]. Because the biological tissue is inherently highly scattering, this physical property strongly attenuates the light along its propagation path, making the OCT signal from deeper depth layers very weak. As a consequence, the sensitivity fall-off at the deeper depth makes SD-OCT harder to detect the weak signals due to this optical attenuation.

The theoretical ranging depth is given by $z_{max} = \lambda_0^2 N/(4n\Delta\lambda)$ [14], where N is the number of sensor elements in the detector. The state-of-the-art SD-OCTA system typically has ~1024 to 2048 pixels, which is possible to achieve ~2 to 7 mm imaging range depending on the design of the spectrometer. Although further depth ranging is possible through full range complex technique [15], the fact that the system sensitivity fall-off adds challenges to image an object with a large depth extend from one part to another, for example, when the imaging of cornea and retina is required in one depth scan, a system that is optimized for cornea in terms of its sensitivity does not necessarily optimized for retina because they are ~24 mm apart in humans.

Secondly, perhaps common to all the current OCT systems, the field of view of the SD-OCTA system is relatively small (typically 3 x 3 mm^2), which is mainly dedicated by the sample arm optics design, imaging speed of the system as well as the requirement of particular applications. Currently, there is a trend to expand further the system field of view to cover wider areas of the target sample. Many OCTA systems take multiple acquisitions and later on, perform montaging of the multiple images to achieve wide FOV, which are however time-consuming and complicated [16]. Often, the imaging requires the re-fixation of the sample to take next image. And moreover, the images resulting from each acquisitions may not be consistent simply due to necessary long acquisition time and sample re-fixation, making it difficult to monitor a dynamic process event. There is one study that reported microvascular imaging with a wide FOV up to 750 mm^2 by the use of SD-OCTA [17].

Biomedical Optics EXPRESS

Although promising, there is an issue for a large sample that is of uneven surface with a depth drop of more than 5 mm from one part to another. However, because of the system sensitivity fall-off as mentioned above, the imaging sensitivity to blood vessels would be different at different depth positions. Ideally, to achieve wide FOV vascular imaging, the system would be best to have a minimum sensitivity fall-off along its depth so that the detection sensitivity to the functional blood vessel at one location is approximately the same as that at another location even if they are more than 5 mm apart in depth. For example, in the imaging of cerebral vasculature within cortical layers of an entire animal, it is often required to monitor the blood flow in anterior cerebral artery (ACA) and middle cerebral artery (MCA) simultaneously. However, because of natural curvature of the brain skull, a depth drop between ACA and MCA is often >5 mm if viewed from top. A promising way to overcome these limitations is to utilize a swept-laser source to implement OCT (i.e., SS-OCT), where time-encoded spectral interferogram signal is obtained through rapidly tuning the narrow line width laser [18].

Recent developments of SS-OCT have proven to offer several advantages over SD-OCT, including its better spectral resolution with reduced sensitivity fall-off, instantaneous sampling of the spectral interferograms that can reduce fringe washout due to motion artifacts from sample or scanner, and dual balanced detection for the reduction of A/D bit depth [19]. One key feature in SS-OCT is the laser technology for the scaling of A-line rates, where the sweeping rate has significantly improved from hundreds kHz [20, 21] to MHz [22, 23] or even multi-MHz [24–26] over the past years. These high-speed laser sweeping technologies are of great importance to reduce the uncomfortable imaging time for patients and provide high spatiotemporal sampling for large FOV functional imaging. In OCTA, system reproducibility is an essential factor that enables the blood flow to be distinguished from static tissue. However, the mechanism of most current swept sources are based on mechanical wavelength scanning techniques such as rotating polygonal mirror [20], piezoelectric-driven Fabry-Pérot cavity [21] and micro-electro-mechanical system (MEMS) actuator [27], which may suffer from severe trigger jitter and phase instability due to the variation of mechanical movement. To improve the phase stability and to synchronize the laser sweeping with the imaging, additional A-scanning trigger, or extra Mach-Zehnder interferometer as an external sampling clock has been proposed to achieve the reduction of the unstable noise for OCT angiography, the strategy of which however increases the system complexity [28]. A promising alternative is to use non-mechanical swept source. Recently, an akinetic swept source based on Vernier-tuned distributed Bragg reflector (VT-DBR) has been reported, which demonstrated excellent coherence length and system stability [29]. The single mode operation of the swept laser provides long coherence length (> 17cm), thus long ranging distance for OCT systems. Its ability of precise programmable control enables unprecedented phase stability (< 2 mrad) and wavelength-tuning repeatability. Perhaps the most attracting is its superior sweeping linearity of the akinetic laser, which makes the requirement redundant of an extra Mach-Zehnder interferometer to provide external optical k-clock. This attribute would certainly simplify the system setup, thus the possible reduction of the system cost.

In this paper, we report the exploration of an akinetic swept source for SS-OCT to achieve long ranging and ultra-wide FOV OCTA (UW-OCTA). To show its advantages in functional ranging and imaging of vascular networks within microcirculatory tissue beds, we provide a comparison between the UW-OCTA and the traditional SD-OCTA through the assessments of basic system sensitivity fall-off and *in vivo* wide-field vascular imaging, where the OMAG images at different depth positions (> 2 cm apart) within the ranging capability of the system are given. Finally, we demonstrate unprecedented, high-quality blood perfusion map within entire human finger achieved by the proposed system through one single 3D scan.

Biomedical Optics EXPRESS

2. Methods

2.1 Experimental UW-OCTA system

Figure 1 illustrates the experimental setup of the UW-OCTA system. The light source employed is an akinetic all-semiconductor programmable swept source (Insight Photonic Solutions, Inc.), which operated at 100 kHz swept rate at 1300 nm central wavelength with 100 nm flat-shaped spectral bandwidth. The axial resolution of this OCT system is ~8 μm. The working principle of this laser is based on Vernier-tuned distributed Bragg reflector (VT-DBR), which enables wavelength selection in the laser cavity by current control. Note that compared to other laser technologies, the akinetic swept source offers several advantages including solid-state wavelength sweeping, mode-hop free single longitudinal mode operation, high sweeping linearity, phase stability, scan repeatability, as well as excellent flexibility for re-programming. It also supplies precise A-line trigger as well as sampling clock to guarantee accurate synchronization of galvo scanning and data acquisition, which is important for OCTA. More details of this akinetic swept source can be found in [29].

In the system, we implemented a fiber-based Mach-Zehnder interferometer by launching the light into a wideband 90:10 coupler. Two optical circulators were employed to route the light into reference arm and sample arm. In the sample arm, we used an additional fiber-coupled laser at 635 nm wavelength to guide the OCT imaging. A pair of XY galvanometric mirrors (Cambridge Technology, 6215H) were synchronized with the akinetic swept source and controlled by a 12-bit high-speed analog output board (National Instruments, PCI-6713). In order to achieve wide-field OCTA imaging, a 2-inch diameter lens with 75 mm long focal length was employed in the sample arm, which provided ~25 μm lateral resolution. The power of the incident light on the sample was 5 mW, leading to a measured sensitivity of ~105 dB. The backscattered light from the two arms were combined and then interfered at a 50:50 coupler. A high-speed dual-balanced photodetector with1.6 GHz bandwidth (Thorlabs, PDB480C-AC) together with a high-speed digitizer (12-bit up to 1.8 GS/s, AlazarTech, ATS9360) were used to detect the OCT interferograms, which provided a system ranging distance of ~46 mm. The raw OCT data was transmitted to a host computer (Intel Xeon 2.4GHz, 128GB RAM) through 8-lane PCI Express Gen2 interface that allowed a maximum data output at rates up to 3.5 GB/s. We developed an efficient program on LabVIEW™ platform to automatically control all the actions of the system including laser sweeping, galvo-scanning, system synchronization, real-time imaging preview and data acquisition.

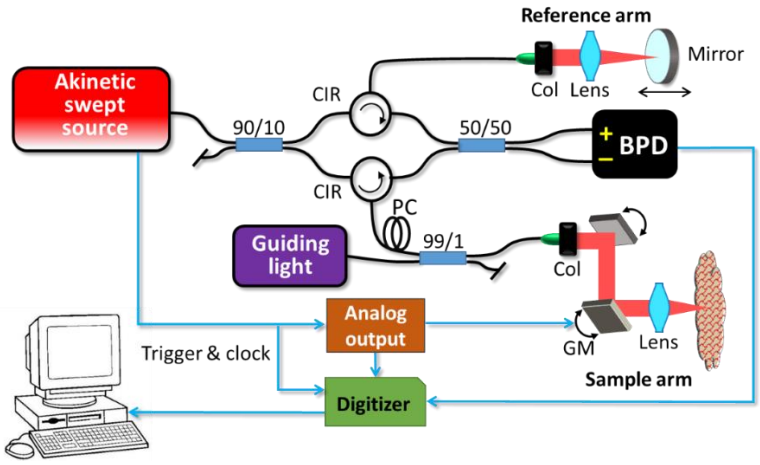

Fig. 1. Schematic of the UW-OCTA system based on akinetic swept source. CIR: circulator, PC: polarization controller, Col: collimator, BPD: balanced photodetector, DAQ: data acquisition.

Biomedical Optics EXPRESS

2.2 Scanning protocols and algorithm to achieve OCT angiography

In this study, we implemented two separate scanning protocols for OCT imaging and ranging of functional vascular networks lying within microcirculatory tissue beds. One is the scanning protocol to achieve OMAG that allows for visualization of the presence and absence of functional blood vessels. The other is the scanning protocol to achieve Doppler OMAG (DOMAG) that allows for the quantitative assessment of the axial components of blood flow of the individual vessels within vascular networks.

In the first scanning protocol, the time interval between the repeated scans at the same location greatly affects the flow sensitivity of OMAG. Here we adopted an ultrahigh sensitive OMAG (UHS-OMAG) scanning protocol to satisfy the requirement of relatively long time interval in high-speed OCT system, which enabled us to image the capillary level microvasculature [9]. In this case, the fast scanner (X direction) was driven by a saw tooth waveform with 200 Hz frame rate, providing 5 ms time interval between adjacent repeated B-scans. Each B-scan image contained 400 A lines that occupied 80% duty cycle. The slow scanner (Y direction) was driven by a step function waveform, which led to 400 B-scan locations with 4 repeated B scans at each step. Thus, each data set of the OMAG contained 640,000 A-lines, taking 8 seconds to complete the data acquisition. The digitizer was operated at its maximum continuous sampling speed of 1.6 GS/s to avoid the error of data overflow. The total size of the data for each session of OMAG imaging is 17.9 GB. After capturing the raw OCT signal, data processing was performed offline to create both the structural and functional blood flow images. The structural images were calculated by averaging the repeated intensity of OCT signals to increase the signal to noise ratio, which can be expressed as Eq. (1):

$$\overline{I(x,y,z)} = \frac{1}{N}\sum_{i=1}^{N} I_i(x,y,z). \tag{1}$$

where $I_i(x,y,z)$ is the amplitude of the OCT signal after Fourier transform in the i'th repeated B scan, N is the number of B-scan repetitions. As the akinetic swept source has superior phase stability, we performed a complex OMAG algorithm by utilizing both amplitude and phase signals to extract the blood flow within the static tissue. The intensity of the blood flow image was calculated by the following equation:

$$I_{OMAG}(x,y,z) = \left[1 - Norm(\overline{I(x,y,z)})\right]\frac{1}{N-1}\sum_{i=1}^{N-1}\left|C_{i+1}(x,y,z) - C_i(x,y,z)\right|. \tag{2}$$

where $C_i(x,y,z)$ is the complex OCT signal containing both amplitude and phase information in the i'th repeated B scan, $Norm(\overline{I(x,y,z)})$ is the normalized structural signals which brings the values in the image to a range from 0 to 1.

In the second scanning protocol that was designed to achieve Doppler OMAG, we utilized the phase information between the adjacent A-scan signals to calculate the Doppler phase shift, upon which to evaluate the axial components of blood flow velocity. In the Doppler measurement, it is known that the flow dynamic range that can be measured by the system is determined by the time interval, Δt, between two A-scans that are used to evaluate the Doppler phase shift due to blood flow [30]. Often, a shorter Δt translates to the system ability to measure faster flows but with a penalty paid for relatively slower blood flows, and vice versa. To serve the purpose of extending dynamic range of flow velocity quantification, a strategy proposed in [31] was adopted by skipping A-scans for evaluating Doppler phase shift. Therefore, in this second scanning protocol instead using repeated B-scans like in the first protocol, we performed repeated A-scans at one location. In this case, the X-scanner was driven by a step function waveform with 500 steps in an entire B-scan, where 50 repeated A-

Biomedical Optics EXPRESS

line scans were collected at each step. We also scanned 500 B-scan planes by applying a step function in the Y-scanner. The total A-line numbers for one DOMAG imaging was as large as 12,500,000. It took ~2 min to complete the data acquisition, which is acceptable to imaging immobilized tissue sample, for example in the small animal models. Under this scanning protocol design, the sampling rate of the digitizer has to decrease in order to avoid the overflow of computer memory. Here we slowed down the digitizer to 500 MS/s, which led to 87.5 GB OCT data for each DOMAG imaging. The detailed algorithm of the DOMAG has been described in [32]. The blood flow velocity along the axial direction was calculated as:

$$v_{axial}(x,y,z)=\frac{\lambda\Delta\varphi(x,y,z)}{4n\pi\Delta t}. \tag{3}$$

where $\Delta\varphi(x,y,z)$ is the mean value of the phase difference between adjacent A-lines, Δt is the time interval between the neighboring A scans that are used for evaluating the Doppler shift and n is the refractive index of the tissue. We also applied a binary threshold mask to reduce the noise background in the Doppler flow images [31].

3. Results

3.1 Sensitivity fall-off performance and comparison

As the signal sensitivity is depth-dependent in OCT system, it is necessary to measure its fall-off performance to evaluate the image quality. Figures 2(a) and 2(b) compare the measured fall-off performance between a traditional spectral-domain OCTA (SD-OCTA) system and the current UW-OCTA system. A broadband superluminescent diode (SLED) centered at 1310 nm with 60 nm FWHM bandwidth was utilized in the SD-OCTA system. We employed a high-speed line-scan camera (Sensors Ltd., GL2048R) running with 2048 pixel-array. The sensitivity of the SD-OCTA system was ~100 dB, which is slightly less than UW-OCTA system due to the loss in detection. We optimized the system to have as long ranging as possible while still maintaining good image quality at higher sensitivity range (i.e. close to the zero delay line) for the purpose of comparison. The axial resolution of the SD-OCTA system is ~9.5 μm. With full spectral span of ~115 nm in the spectrometer, the spectral resolution is ~0.078 nm which is determined by the camera, grating, lens, incident angle and size of the beam. This configuration gives 7.5 mm imaging range as shown in Fig. 2(a) where a more than 30 dB signal drop at the maximum imaging range of 7.5 mm is seen compared to that of zero delay line. For the UW-OCTA system, the digitizer was run at 1.6 GS/s, which produced ~16 k sampling points per A-line. Due to the invalid transition intervals in the laser sweeping that has been described in [29], we discarded the invalid data by utilizing the "data valid vector" (DVV) provided by the akinetic laser. In this case, the number of the effective data or valid data was 10,108 per A-line, leading to a maximum axial depth of 46 mm. Due to the single mode operation in the akinetic swept source, the instantaneous linewidth is extremely narrow. Moreover, with precise control of the driving voltage, the light source demonstrates unprecedented sweep linearity which greatly simplifies the system setup because there is no need to have an external k-clock to stabilize and synchronize the data acquisition [29]. Under this circumstance, the measured system sensitivity fall-off is shown in Fig. 2(b), without any attempt for calibration to enhance the signal, where it is seen that the sensitivity of the UW-OCT system has merely ~3 dB fall-off within the ranging distance of 46 mm, demonstrating much better fall-off performance compared to that of the SD-OCT. It should be noted that the coherence length of the akinetic swept source far exceeds the maximum depth that we can achieve in this setup. The small sensitivity fall-off is mainly due to the slightly nonlinear sweeping of the akinetic laser in high frequency region. The demonstrated ranging of 46 mm is limited by the 1.6 GHz A/D digitizer used in this study. The red arrows in Fig. 2(b) point to some of representative ghost peaks of the PSF curves. For better illustration, we selected two of the measured point spread function (PSF) at the depth positions of ~6 mm and ~8 mm,

Biomedical Optics EXPRESS

respectively, and plotted them in frequency domain as shown in Fig. 2(c). The ghost peaks (pointed by red arrows in Fig. 2(c)) are the mirror images mirrored from the negative frequency domain, which is 800 MHz far from the main peaks. These ghosts are likely due to electronic harmonics introduced by the 400 MHz driving clock of the swept laser. While the distance of the reference mirror increases, there is also a small rise of the noise floor that may be due to the unperfected sweeping linearity in the akinetic source. Nevertheless, considering the fact that the OCT imaging depth in the biological tissue is typically less than 3 mm, these artifacts would not have noticeable effects on the actual OCT images, since the ghost image is usually far away from the real position and the noise floor is generally ~30 dB weaker than the sample signal. These results demonstrate that UW-OCTA is much more favorable over the SD-OCTA for the wide-FOV imaging of a large target sample with uneven surface.

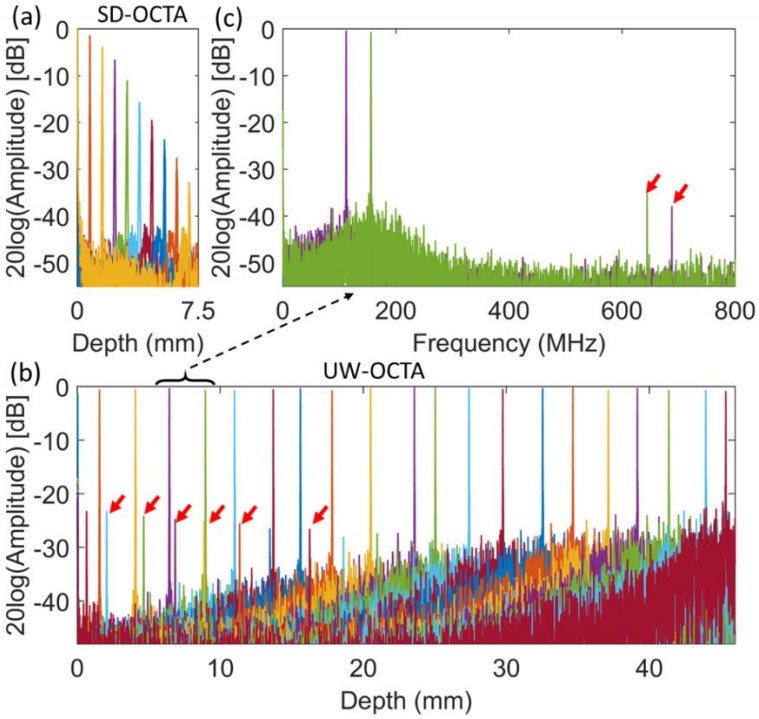

Fig. 2. System sensitivity fall-off assessment over its ranging distance. (a) The SD-OCTA system with spectrometer detection and (b) the UW-OCTA system with the akinetic swept source. (c) Two typical point spread function (PSF) measurements at the ranging distance of ~6 mm and ~8 mm, respectively. Note that the x axis in (c) is labeled in the frequency domain, instead of distance. The red arrows in (b) point to some of the representative ghost peaks. The red arrows in (c) point to the ghost peaks of the two selected PSF measurements.

3.2 Functional wide-field OCT imaging and comparison

After the assessment of sensitivity fall-off over a ranging distance of 46 mm in our proposed UW-OCTA system, we further demonstrate its capability of wide-field imaging and ranging of functional vascular networks. We further compare the vascular imaging performance to that of SD-OCTA. In this part of the study, we used the systems to image entire cerebral vascular networks within cortical layers of a mouse brain with its cranium left intact. In order to make relatively fair comparison, we utilized the same fiber-based OCT interferometer by just switching the light source and detection for the two OCTA systems. Both of them had the same imaging speed, i.e. 100 kHz A-line rate, and similar power incident on the sample, which was ~5 mW. The mouse we used in the study was a three-month-old C57/BL6 mouse weighing ~24g purchased from Charles River Laboratories. During imaging, the animal was

Biomedical Optics EXPRESS

anesthetized by inhaling isoflurane at 1.5% concentration with 0.2 L/min O_2 and 0.8 L/min air. The mouse was kept by a heating pad to maintain its body temperature. A simple surgery was conducted to expose the entire skull of the mouse brain by shaving the hair and retracting the scalp. After adding several drops of saline, we covered the entire open skull with a plastic wrap to maintain the hydration of the skull bone during imaging. To reduce breathing motion artifacts, the head of the mouse was immobilized in a custom-made stereotaxic stage. All experimental animal procedures prepared for this pilot study of imaging were reviewed and approved by the Institute of Animal Care and Use Committee of University of Washington (Protocol #: 4262-01).

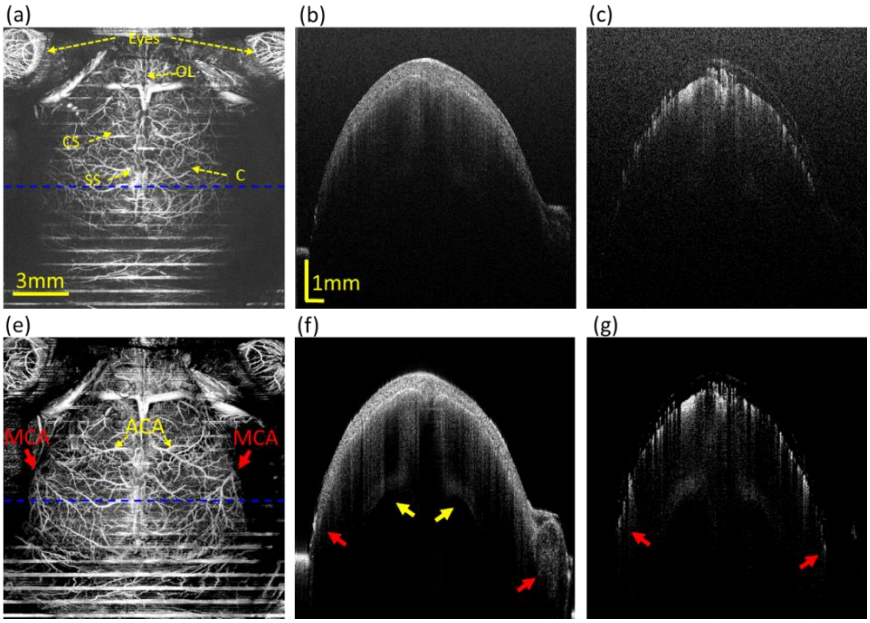

Fig. 3. The OMAG images of the entire mouse brain with the cranium left intact captured by SD-OCTA system (top row) and UW-OCTA system (bottom row), respectively. (a) and (e) are the *en face* MIP cerebral vascular images. (b) and (c) are the cross-sectional structural and vascular images at the position indicated by the blue dash line in (a) by SD-OCTA. (f) and (g) are the corresponding cross-sectional image pairs at the position indicated by the blue dash line in (e) by SS-OCTA. The yellow arrows in (f) point out the structure of corpus callosum. The red arrows in (e-g) indicate structure and blood vessels at deep positions of mouse brain which is not clear or absent in (a-c). OL: olfactory lobes, CS: coronal suture, SS: sagittal suture, C: cerebellum, MCA: middle cerebral arteries, ACA: anterior cerebral artery.

Figures 3(a) and 3(e) show the *en face* maximum intensity projections (MIP) of the vascular networks in the cortical layers of brain obtained by the SD-OCTA system and the UW-OCTA system, respectively. The imaging FOV for both the systems was as large as ~15 × 15 mm^2, which enables the visualization of eyes, olfactory lobes, bregma, coronal suture, sagittal suture and cerebellum in one scan. As for wide-field imaging, the depth locations of different biological tissues could vary from several millimeters to even centimeters in bulk sample. In the OMAG image of SD-OCTA system (Fig. 3(a)), the blood vessels in the middle part of mouse brain are close to zero delay line in the OCT images, thus giving better contrast and clarity. However, due to the poor fall-off performance in the SD-OCTA system, although the vessels in the peripheral area of the mouse are still within the imaging range, the weak OCT signals in the deep axial positions, e.g. those pointed by arrows, make them difficult to be visualized because of the low image contrast resulted by the relatively low detecting sensitivity. Thanks to the single mode operation of the akinetic swept source and the high-speed sampling rate of the digitizer, we were able to achieve high quality images for the parts

Biomedical Optics EXPRESS

located at deep axial position without much compromise of signal fall-off. As pointed by the red arrows in Fig. 3(e), the UW-OCTA system provides clear visualization of the blood vessels and the associated networks at the territory of middle cerebral arteries (MCA), which are located at quite low positions of the left and right side in the mouse brain. It should be noted that the vessels of MCA are the main channels to supply the brain, which are of great value for the study of neurovascular disorders like stroke. The horizontal white lines in the *en face* MIPs are originated from the breath motion artifacts. Figures 3(b), 3(c) and (f,g) are the 2D cross-sectional structure and corresponding blood flow images at the positions indicated by the blue dashed line in Figs. 3(a) and 3(e), respectively. It is obvious that the cross-sectional images of the structure and blood flow captured by the UW-OCTA system have higher image contrast and signal-to-noise ratio (SNR) than those by the SD-OCTA system. The structural image in Fig. 3(f) demonstrates better structure connectivity (pointed out by the left red arrow) and provides more internal details (pointed by the right red arrow) at deep axial positions. The results demonstrate that UW-OCTA system is capable of imaging not only the superficial structure of mouse brain including the bones, meninges and cortex, but also the structure of corpus callosum (pointed out by the yellow arrows in Fig. 3(f)) located at a position as deep as ~2 mm below the skull layer. As a consequence, the vascular imaging by UW-OCTA system enables the visualization of the blood vessels in deep axial position as pointed out by the red arrows in Fig. 3(g), which are however absent in the SD-OCTA system.

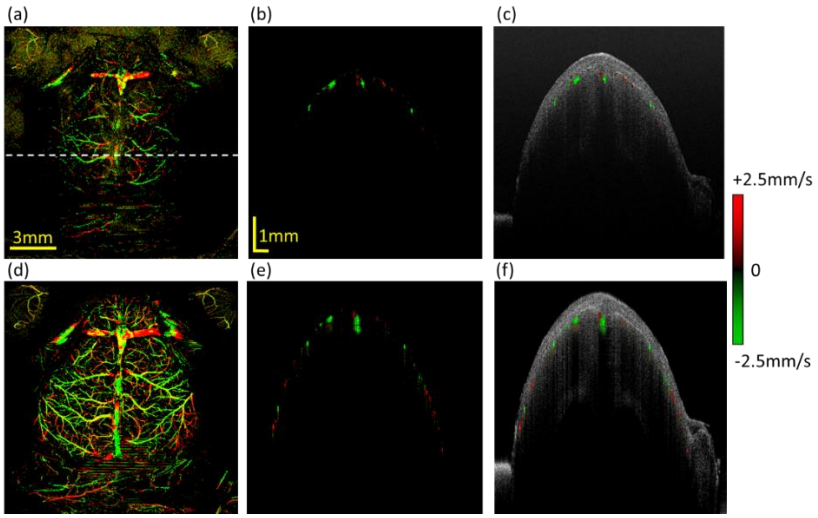

Fig. 4. The comparison of wide-field DOMAG imaging of entire brain with cranium left intact between SD-OCTA system (top row) and UW-OCTA system (bottom row). (a) and (e) are the *en face* Doppler cerebral vascular images. (b) and (c) are the cross-sectional Doppler flow image alone and the Doppler flow image overlaid with structural image at the position indicated by the white dash line in (a) by SD-OCTA. (f) and (g) are the corresponding comparison pairs at the position indicated by the white dash line in (d) by SS-OCTA.

In addition, we also performed *in vivo* experiments to compare the wide-field Doppler OMAG (DOMAG) performance between the two OCTA systems. The DOMAG imaging protocol and algorithm have been described in section 2.2. Unlike the OMAG method that averages the signal difference among the repeated B scans, DOMAG calculates the averaged phase shift between adjacent A scans in the M-mode scan, making the blood flow imaging in DOMAG less sensitive when compared to the OMAG method in terms of visualizing functional blood vessels. Thus compared to Fig. 3(a), the DOMAG vascular image captured by the SD-OCTA system has more phase noise and less network connectivity (shown in Fig. 4(a)). As shown in the cross-sectional Doppler blood flow image (Fig. 4(b)) and the

Biomedical Optics EXPRESS

combination of Doppler blood flow image and structural image (Fig. 4(c)), the OCT signal at left and right side of brain is weak and the corresponding Doppler signal is invisible at the deep axial locations. In contrast, the *en face* MIP DOMAG (Fig. 4(d)) created by the UW-OCTA system shows the integrity of the entire vascular networks of mouse brain with quantitative axial flow information. The cross-sectional Doppler flow image (Fig. 4(e)) clearly demonstrates a plenty of blood vessels not only in the middle region of mouse brain but also in the peripheral regions of the mouse brain. With the aid of structural image, the overlaid image (Fig. 4(f)) helps us better identify the precise position of these blood vessels. The capability of wide-field DOMAG imaging with ultrahigh blood flow sensitivity provided by the UW-OCTA system enables us to visualize and quantify the entire vascular networks of the mouse brain, an important ability in the investigations of vascular involvements in neurological conditions that may provide useful information to aid the diagnosis, treatment and management of neurovascular diseases.

3.2 Long-range OMAG imaging

From above, the UW-OCT has been demonstrated to be superior in terms of sensitivity fall-off along the 46 mm ranging distance. It would be useful to verify its ability in imaging the cerebral vasculature if the target is situated at different ranging depth positions. Due to the limitation of the Gaussian optics design in the sample arm of our system, the depth of focus was around ~2.3 mm, meaning the lateral resolution worsens at the ranging position outside this depth of focus. To alleviate this issue of Gaussian optics, we opted for changing the position of the reference mirror while the sample was fix-located within the depth of the focus. Thus, by moving the reference mirror on a precision optical rail, it simulates the situation as if the ranging position of the mouse brain in the OCT image is changed during the experiments. In addition, this way of handling also ensures that the optical illumination onto the sample was constant throughout the experiments, eliminating the effects of different lateral resolution on the final vascular image quality when the sample is located at different depth locations, which serves our purpose well in the test of UW-OCTA's ability of ranging vascular features.

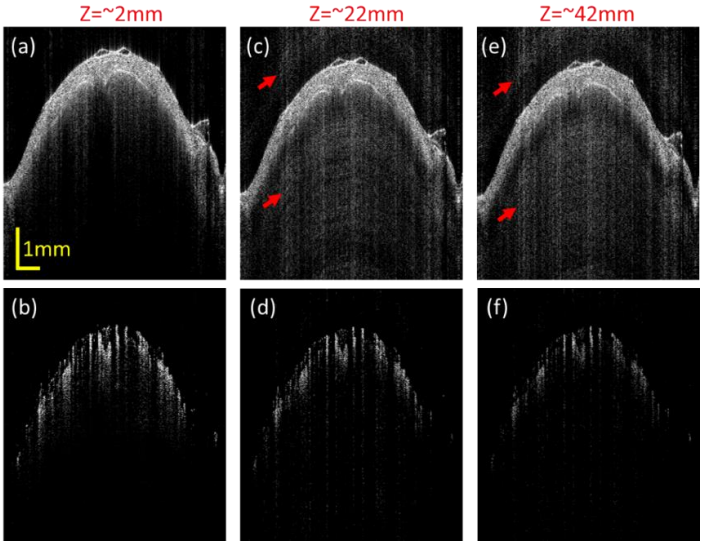

Fig. 5. Representative B-scan structural images (top row) and corresponding blood flow images (bottom row) of mouse brain with the cranium left intact when the animal was positioned at the ranging distances of 2 mm (left column), 22 mm (middle column) and 42 mm (right column), respectively. The arrows in (c-e) point out the ghost artifacts due to the rise of side lobes.

Biomedical Optics EXPRESS

Figure 5 shows the 2D B-scan structural images and corresponding vascular images of the mouse brain when the animal was located at different ranging positions allowable by our system. The images of Figs. 5(a) and 5(b), which are close to zero delay, provides the best image quality for structural and vascular visualization. As shown in Fig. 5(c)-5(f), while the ranging position was increased to ~22 mm and ~42 mm, the imaging performance of structural and vascular images are still high enough to identify different tissue structures and blood vessels without severe sensitivity fall-off and resolution degradation, as expected. Due to slight rise of side lobes at the deep axial positions, there are some ghost signals that appear in the structural images as shown in Fig. 5(c) and 5(e) (pointed by arrows). Nevertheless, the ghost artifacts do not significantly degrade the OCT image quality. However, it is noticeable that the intensity of both structural and functional images becomes increasingly weak with the increase of the ranging depth position. This is due to gradual sensitivity fall-off over the ranging distance even though that fall-off is small (~3dB at the 46 mm ranging depth).

Figure 6 shows the corresponding *en face* MIPs of the cerebral blood flow images when the animal was positioned at 2 mm, 22 mm and 42 mm, respectively. Although there is a slight decrease in the brightness due to the small sensitivity fall-off, these *en face* vascular maps are of similar quality, and all of them can clearly identify various physiologically important features of cerebral blood vessels within mouse cortex, including superior sagittal sinus, transverse sinus, middle cerebral artery (MCA) and anterior cerebral artery (ACA). These imaging results agree well with the fall-off measurement as shown in Fig. 2(b), sufficiently demonstrating the strength of UW-OCTA system for functional vascular ranging and imaging without strict limitation of sample locations relatively to the OCT probe, which would be clinically important for wide FOV imaging of body parts where the surface is unlikely even, for example the entire finger or hand.

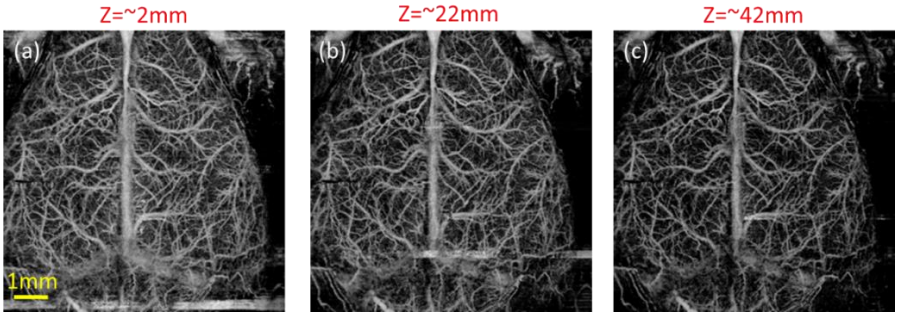

Fig. 6. The *en face* cerebral vascular images of mouse cortex when the animal was positioned at the ranging positions of (a) 2 mm, (b) 22 mm and (c) 42 mm, respectively.

3.4 Wide-field OMAG imaging of entire finger for dermatology applications

Apart from applications in neuroscience that the UW-OCTA system could offer, there is also an increasing interest in the field of dermatology to visualize the cutaneous microcirculation as well as the tissue structure with wide FOV imaging to aid the disease diagnosis and monitoring the therapeutic treatment. Here, we demonstrate the capability of our proposed UW-OCTA for *in vivo* OMAG imaging of an entire human finger in a human volunteer, a body part that is perfused with rich blood, thus with dense microvascular networks within cutaneous tissue beds. To minimize the hyper-reflection of the skin-air interface, we applied a drop of glycerol solution spread thinly over the skin surface of a ring finger for refractive-index matching [33]. Figure 7(a) shows the top-view structural image of the ring finger of the right hand. The FOV was as wide as 23 × 18 mm^2, which is sufficient to cover the entire nail fold region and the peripheral tissue area including the distal edge, nail plate, lateral nail folds, lunula, cuticle, eponychium and proximal nail fold. Figure 7(b) is the corresponding *en face* vascular image, where we can clearly observe the delicate vascular networks that

Biomedical Optics EXPRESS

function to supply the energy and nutrition for finger activities. The blood vessels vary with different patterns and diameters at different parts of the finger, that correspond well with the descriptions in typical anatomy text book. With the help of the structural image to identify the surface outline of the finger, a vascular map of the blood vessels was created with color coding in terms of the depth starting from the tissue surface (shown in Fig. 7(c)), which is a useful presentation to appreciate the depth locations of the blood vessels. We are able to clearly visualize the big vessels growing from deep dermis layer (> 1 mm depth), which are then split into smaller branches in the superficial skin layer in the region of the proximal nail fold. The blood vessels in the nail plate region can be easily distinguished by the color, since they only grow under the nail plate that has ~1 mm thickness. Due to the superior imaging performance, this UW-OCTA system is capable of capturing some vessels in the deep region of ~2 mm in depth as shown by the red color in Fig. 7(c). To investigate in more detail, a boundary region between nail plate and distal edge is zoomed in Fig. 7(d) for scrutinizing the microvascular patterns and features. Most of the blood vessels under the nail plate grow in horizontal direction along the fingertip while the vessels in the distal edge of the ring finger contain rich hair-pin like capillary loops, almost perpendicular to the surface.

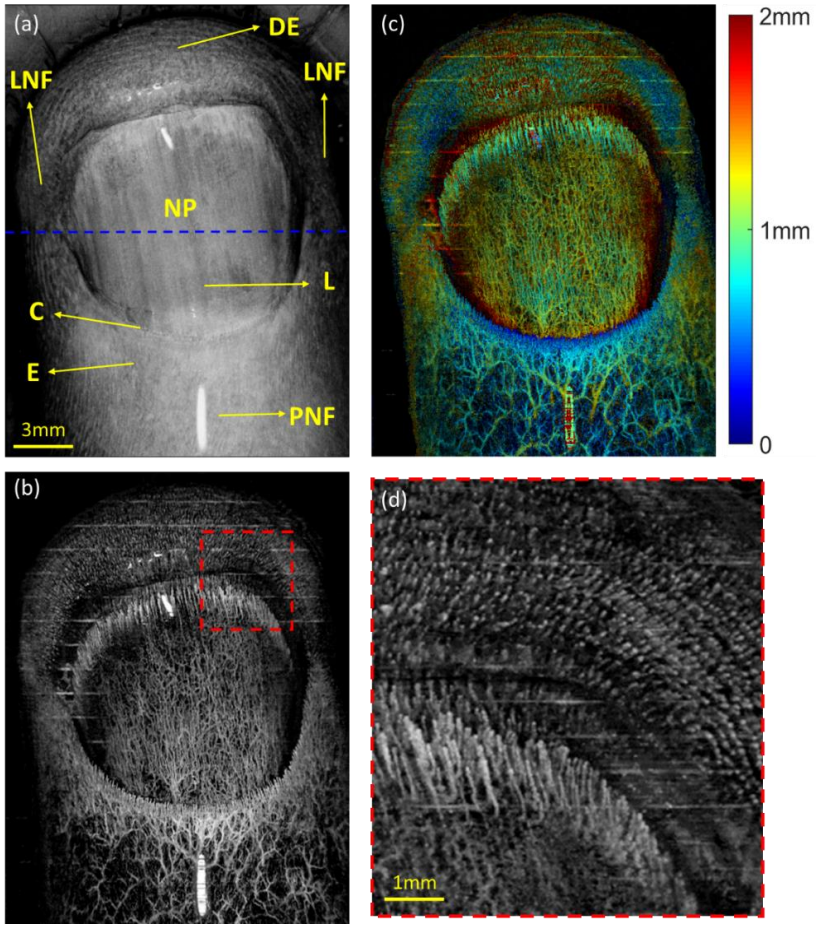

Fig. 7. *in vivo* wide-field OMAG images of the entire ring finger of a human volunteer. (a) The top-view structural image. (b) The corresponding *en face* microvascular image. (c) The *en face* microvascular image with depth-color coding to appreciate the depth location of the blood vessels. (d) The zoom-in *en face* vascular image in the region indicated by the red dashed box in (b). DE: distal edge, LNF: lateral nail fold, NP: nail plate, L: lunula, C: cuticle, E: eponychium, PNF: proximal nail fold.

Biomedical Optics EXPRESS

Figure 8 shows the representative B-scan images of structure and vasculature at the position indicated by the blue dashed line in Fig. 7(a). In the structural image as shown in Fig. 8(a), multiple layers including the nail plate, nail bed and dermis are clearly identified in the nail fold region. Thanks to the long ranging and superior fall-off performance provided by the UW-OCTA system, the cross-sectional morphology of lateral nail folds at the deep axial position of > 2mm away from the tissue surface is still visible. As shown in Fig. 8(b), the high structural and functional sensitivity provided by the system enables us to visualize the deeply localized blood vessels despite of the thick nail plate and lateral nail fold. After fusing the blood flow with the structural image, Fig. 8(c) provides better interpretation for cutaneous microcirculation with anatomical orientation. These functional results demonstrate potential clinical value of the UW-OCTA in the aid of the diagnosis of vascular involvements in skin related diseases, including inflammation and diabetes.

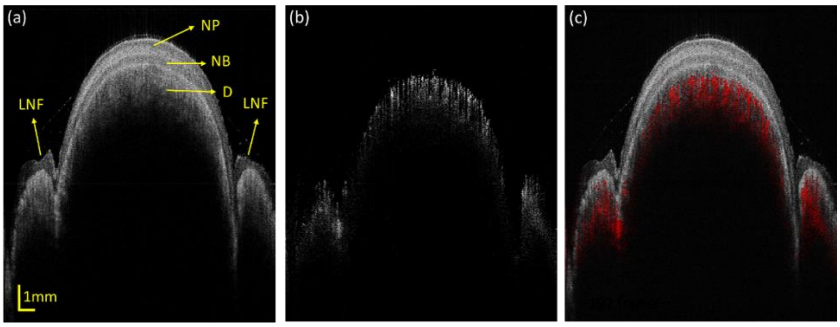

Fig. 8. Typical cross-sectional structural and corresponding blood flow images at the position indicated by the blue dashed line in Fig. 7(a). (a)The structural and (b) the corresponding blood flow images, respectively. (c) The combined structural image (grey color) and blood flow image (red color). NP: nail plate, NB: nail bed, D: dermis, LNF: lateral nail fold.

4. Discussion and conclusion

We have shown that our UW-OCTA system based on akinetic swept source and high-speed detection has the advantages of long ranging distance of 46 mm with a merely 3 dB sensitivity fall-off. The 46 mm ranging was achieved by sampling the spectral interferogram using a digitizer capable of 1.6 GHz sampling rate. It is noteworthy that the coherence length of the akinetic swept source far exceeds the maximum depth allowed by the system. By reducing the swept rate and swept bandwidth, or employing faster digitizer, the imaging distance could be further extended to tens centimeters or more. The small sensitivity fall-off over 46 mm ranging is due to the improved detection efficiency by the balanced detector and narrow instantaneous linewidth provided by the single mode operation of the laser source. These attributes are particularly important for clinical imaging applications where 1) it requires to image the microstructure and microvasculature at the body parts that are located far apart in terms of depth extend, and 2) it requires improved contrast of vascular features located at deeper depth.

Note that the improvement of system sensitivity and the ability to perform long distance ranging do not necessarily mean that the imaging depth of OCT and OCTA is increased. From biomedical optics, we know that the OCT signal from deeper depths is inherently weak due to the exponential decay of light when propagating along its path. This physical property puts a hard limit of ~2 mm imaging depth for OCT and OCTA, at least for the wavelength ranges currently used for OCT implementation. However, the improvement of system sensitivity would serve to better detect the very weak signals emerged from the deeper depth of tissue. This attribute, combined with long ranging distance, would be particularly beneficial for wide-field OCTA ranging and imaging of microvascular features of relatively large tissue sample.

Biomedical Optics EXPRESS

Another important feature of the akinetic light source is its outstanding phase stability and sweeping repeatability and linearity, which plays an important role in the reconstruction of highly sensitive, functional vascular images. Its stability and linearity would also enable a number of advantages for OCTA. First, it is not necessary to have a purposely designed auxiliary interferometer for the purposes of re-calibrating the interferograms, leading to stable, simple and economic system setup. Secondly, it enables highly sensitive complex OMAG algorithm, i.e. utilizing both the amplitude and phase of OCT signals, to create high-contrast vascular maps. And thirdly, it facilitates the Doppler OMAG imaging to provide quantitative information of vascular blood flow velocities, albeit the axial components. As demonstrated by vascular imaging of an entire mouse brain, the UW-OCTA system provided superior performance of quantitative wide-field functional imaging of blood flow to that of the traditional SD-OCTA system. The full map of the cerebrovascular networks in the cortical tissue of mouse brain could serve as a potential and powerful inspective tool for a variety of neurological studies such as stroke, traumatic brain injury and Alzheimer.

In this study using the UW-OCTA system, we also succeeded to achieve unprecedented blood perfusion map of human finger with the FOV as wide as 23 × 18 mm^2, which covered the entire nail fold region as well as the peripheral area. The clear visualization of the vascular networks in human finger indicates a promise for various clinical applications in dermatology.

Although this UW-OCTA system demonstrates a number of advantages, future developments for clinical translation require to overcome the challenges to handle the big data flow and to reduce data acquisition time to a range that is comfortable for patient imaging (typically less than 5 sec). In our experiments, each OMAG measurement contains 400 A lines and 400 B scans with 4 repetitions, which generates 17.9 GB raw OCT data. Whereas for the quantitative assessment of flow speeds, the Doppler OMAG requires more repetitions, leading to a data size as large as 87.5 GB for one 3D scan. With wide FOV, more number of pixels in the image is needed to avoid undersampling which may further increase acquisition time and data size. Although the functional sensitivity might be compromised, reducing the scanning repetitions has been proven as a feasible way to compress the data size as well as the data acquisition time for wide-field imaging [34]. Nevertheless, with the rapid development of computing technology, e.g. GPU and FPGA, that is hopeful to seamlessly improve data storage, data transition, data computation, and thus the pressure due to the large data size for wide-field functional imaging may be reduced in a not far distance future. Besides, it is also important to consider the data acquisition time for clinical applications because long imaging time can introduce motion artifacts in the final angiograms, and affect the patient compliance for imaging. Our OMAG imaging takes several seconds which is acceptable for clinical practice, while the data acquisition for Doppler OMAG is relatively long (~2 min). One way to improve this situation is to use faster sweeping rate of the light source. Fortunately, a faster version of akinetic swept source with 200 kHz speed has been reported for OCT angiography recently [35]. Without the mechanical scanning movement, future development of this akinetic technique for up to MHz sweeping rate is believed to be feasible. Instead of relying on future work to increase the swept rate of the light source as well as speed up the scanning and detection system, another practical alternative to reduce the total imaging time is to perform parallel imaging through multiple channels, with each channel targeted to different regions of the sample. The technique of multi-spot illumination has been reported to greatly improve the 2D depth scan line rate in FDML-OCT system [24].

In summary, a long ranging and wide-field OCT angiography system has been developed by employing superior akinetic swept source together with high-speed detection of OCT interference signals. We have shown that the proposed UW-OCTA is capable of unprecedented imaging and ranging (up to 46 mm) of functional blood vessels within microcirculatory tissue beds with almost negligible sensitivity fall-off (only 3dB at 46 mm). The high phase stability and sweeping linearity and repeatability of the akinetic light source

Biomedical Optics EXPRESS

have shown to be responsible for high-sensitive functional imaging using complex OMAG and Doppler OMAG. We further verified the capability of long ranging in UW-OCTA system when the mouse brain is positioned at various depth positions for up to 42 mm. Finally, these demonstrated advantages of the UW-OCTA system helped us succeed a remarkable wide-field blood perfusion map in the human finger, illustrating the rich blood vessels wired from the superficial skin layer to the deep dermis tissue. The results indicate a promise for the translation of UW-OCTA to the fields of, among other fields, the neuroscience for the investigation of vascular involvement in neuro-diseases, and the clinical dermatology for imaging skin vascular features in subcutaneous beds.

Funding

This work was supported in part by grants from the National Heart, Lung, and Blood Institute (R01 HL093140) and the National Eye Institute (R01 EY024158).

Acknowledgments

We acknowledge Michael Minneman, Erich Hoover, Jason Ensher and Simon Gray from Insight Photonic Solutions, Inc. for providing the light source used in this study, and their support and help to operate the light source.